

Closely spaced co-rotating helical vortices: General solutions

A. Castillo-Castellanos and S. Le Dizès

*Aix Marseille Université, CNRS, Centrale Marseille, IRPHE, Marseille, France**

E. Durán Venegas

Aix Marseille Université, CNRS, Centrale Marseille, IRPHE, Marseille, France and
Departamento de Bioingeniería e Ingeniería Aeroespacial, Universidad Carlos III de Madrid, Spain*

(Dated: July 28, 2022)

In this work, we present general solutions for closely spaced co-rotating helical vortices using a filament approach. For these vortex structures, helical symmetry is broken, but solutions maintain a form of spatial periodicity. We show there exists a moving frame where vortex elements move along the structure without distorting it. These solutions can be used to characterize the evolution of the twin-tip vortices produced in the wake of a tip-splitting rotor blade. The resulting wake has a dual nature. Locally, the structure behaves much like an helical pair aligned with the locally tangent flow. However, as we move away from the vortex structure the induced flow is reminiscent of an ‘equivalent’ helical vortex with thicker core.

I. INTRODUCTION

Rotating blades, such as those of a helicopter rotor or a horizontal-axis wind turbine, generate concentrated vortices at their tips, transported downstream, creating a persistent helical pattern. These helical vortices are associated with several practical issues actively investigated today. One of these issues concerns the interaction between a tip vortex and a rotor blade (Blade-Vortex Interaction, BVI), which causes significant noise and vibration problems. BVI is responsible for premature structural component fatigue in wind turbines and undesirable noise in helicopter rotors during low speed and descending flight [1]. In general, there are two kinds of BVI mitigation strategies: active and passive [2–4]. Active methods include dynamical modifications of the blade geometry or the local boundary layer through actuator systems. Passive methods use a blade geometry designed to enhance particular flow features, for instance, by introducing serrations on the leading edge [5, 6] or through the use of winglets [7, 8]. One alternative proposed by Brocklehurst and Pike [9] is to use a modified airfoil to split the tip vortex into two closely spaced vortices. This approach offers significant noise reduction and has no adverse effects on control load or performance. Our objective is to provide the structure of the wake produced by a tip-splitting rotor for wind turbine and helicopter regimes.

Previous studies focused on the mechanical and acoustical response of a vortex pair impinging on an airfoil either through wind tunnel measurements [10, 11] or numerical simulations coupled with aero-acoustical models [12, 13]. In the wind turbine community, blade loading is usually obtained using the Blade Element Momentum (BEM) theory. This involves obtaining the angle of attack and airfoil data from experimental measurements or computations (see, for instance [14]). Blade loading may also be obtained from prescribed wake models. However, prescribed wake models often neglect the radial contraction (resp. expansion) observed in helicopter flight (resp. wind turbine) regimes. Recently, Durán Venegas *et al.* [15] proposed an alternative approach to estimate blade loading by finding stationary solutions of Joukowski’s rotor wake model for all helicopter flight and wind turbine regimes. In this approach, the following considerations are made: (i) vortices roll-up quickly to form thin vortex filaments of small but finite core size; (ii) velocity induced by the filaments is described by Biot-Savart with a cut-off approach, and (iii) vortex filaments are force-free and convect with the local velocity. In Joukowski’s rotor wake model, we expect the solutions to match uniform helices in the far-field. While these structures have been the subject of an enormous amount of works going back to Kelvin [16] and Da Rios [17], solutions for tip-splitting rotors are not available in the literature.

The closest canonical example to these closely spaced co-rotating helical vortex pairs is a pair of equistrength parallel vortices. In such a case, the parameters driving the vortex dynamics are the circulation Γ , separation distance d , and vortex core size a . In general, a grows with time due to viscous diffusion of vorticity with $a(t) = \sqrt{4\nu t + a_0^2}$ where ν is the kinematic viscosity, while d remains virtually constant. Simultaneously, the vortex pair rotates around the total vortex centroid with constant rotation rate $\omega = \Gamma/(\pi d^2)$. When the ratio a/d exceeds a threshold value, d suddenly decreases and the vortices merge into a single entity (see, for instance [18–22]). Given the separation of

* andres-alonso.castillo-castellanos@univ-amu.fr

scales, we expect the closely spaced helical pairs to display similar properties. The development of long-wave and short-wave elliptical instabilities [23–26] also has practical relevance, since these instabilities may enhance vortex diffusion, accelerate the merging process and the transition towards a turbulent wake.

The paper is organized as follows. Section II briefly introduces the vortex filament framework used. Section III is concerned with the far-field. We show how stationary but spatially-periodic solutions are obtained from a few geometric parameters. In section IV, these solutions are then used to compute the far-field contribution for the near-field solutions obtained close to a tip-splitting rotor. We present solutions representative of both wind turbine and helicopter regimes and discuss the rotor influence on the wake structure. We also provide a simple model explaining the observed spatial variations of the parameters.

II. FRAMEWORK

The present work is based on a vortex filament approach. We then consider thin vortices for which the core size is small compared to the other spatial scales (separation distances, local curvature radius). Our framework is the same as used in [15, 27]. All the vorticity is considered as being concentrated along lines which move as material lines in the fluid according to

$$\frac{d\mathbf{X}_i}{dt} = \mathbf{U}(\mathbf{X}_i) + \mathbf{U}^\infty \quad (1)$$

where \mathbf{X}_i is the position vector of the i -th vortex filament, \mathbf{U} the velocity induced by the vortices and \mathbf{U}^∞ an external velocity field. The induced velocity \mathbf{U} is given by the Biot-Savart law

$$\mathbf{U}(\mathbf{X}_i) = \sum_{j=1}^n \frac{\Gamma_j}{4\pi} \int \frac{(\mathbf{X}_j - \mathbf{X}_i) \times d\mathbf{T}_j}{|\mathbf{X}_j - \mathbf{X}_i|^2} \quad (2)$$

where the integrals cover each vortex filament defined by its circulation Γ_j , position vector \mathbf{X}_j and corresponding tangent unit vector \mathbf{T}_j . The divergence of Biot-Savart integral on the vortices is treated using the cut-off method with a Gaussian vorticity profile [28]. Each vortex filament is discretised in segments $[\mathbf{X}_i^n, \mathbf{X}_i^{n+1}]$ in order to compute the velocity field and follow its evolution. The discretised expressions that we shall use for the induced velocity are given in [27].

Our objective is to find a vortex structure that is steady in the frame of the rotor. This condition of steadiness reads as

$$(\mathbf{U}(\mathbf{X}_j) - \mathbf{U}^F) \times \mathbf{T}_j = 0 \quad (3)$$

where \mathbf{U}^F is the frame velocity, which simply indicates that vortices are moving along the vortex structure. In practice, we shall write the steadiness condition as a system of ordinary equations. In a cylindrical frame, it can be written for each vortex as

$$\frac{dr_j}{d\zeta} = U_r(\mathbf{X}_j), \quad \frac{d\theta_j}{d\zeta} = \Omega(\mathbf{X}_j) - \Omega^F, \quad \frac{dz_j}{d\zeta} = U_z(\mathbf{X}_j) - U_z^F, \quad (4)$$

where $(r_j(\zeta), \theta_j(\zeta), z_j(\zeta))$ are the radial, angular, and axial coordinates of the j -th vortex, $(U_r, r_j\Omega, U_z)$ the corresponding velocity components, while Ω^F and U_z^F are the angular and axial velocity of the rotor frame. Each vortex curve is parametrized by ζ . These systems are to be solved with boundary conditions on the rotor, at $\zeta = 0$, where the position of each vortex is prescribed, and far-field boundary conditions at $\zeta \rightarrow \infty$.

These last boundary conditions are not trivial as the far-field is a priori unknown. Therefore, our first task is to characterize the far-field.

III. FAR-FIELD SOLUTIONS

We are interested in solutions that are created by the emission of two closely-spaced co-rotating vortices from a rotating blade tip under an external axial flow. Based on the observation of the tip vortices [29], one may naturally expect close to the rotor, a global contraction of the structure in a climbing helicopter regime, and a global expansion in a wind turbine regime. In the far-field, a quasi-uniform regime is expected. However, this regime is not as simple as for a single tip vortex. We shall see that while not perfectly uniform, the vortices deform but exhibit a certain periodicity induced by their mutual interaction. The description of this far-field can be analyzed using the method introduced in [27] for counter-rotating helical vortices. These solutions are defined only by the geometrical parameters introduced in the following section.

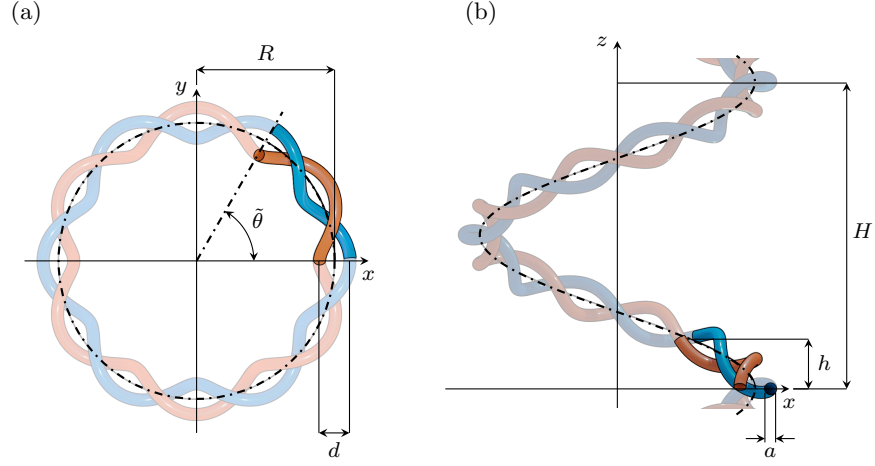


FIG. 1. Geometric parameters of closely spaced tip vortices: separation distance d , radius R , vortex core size a , axial pitches H and h , and twist parameter $\beta = \pm 2\pi/\tilde{\theta} = H/h$.

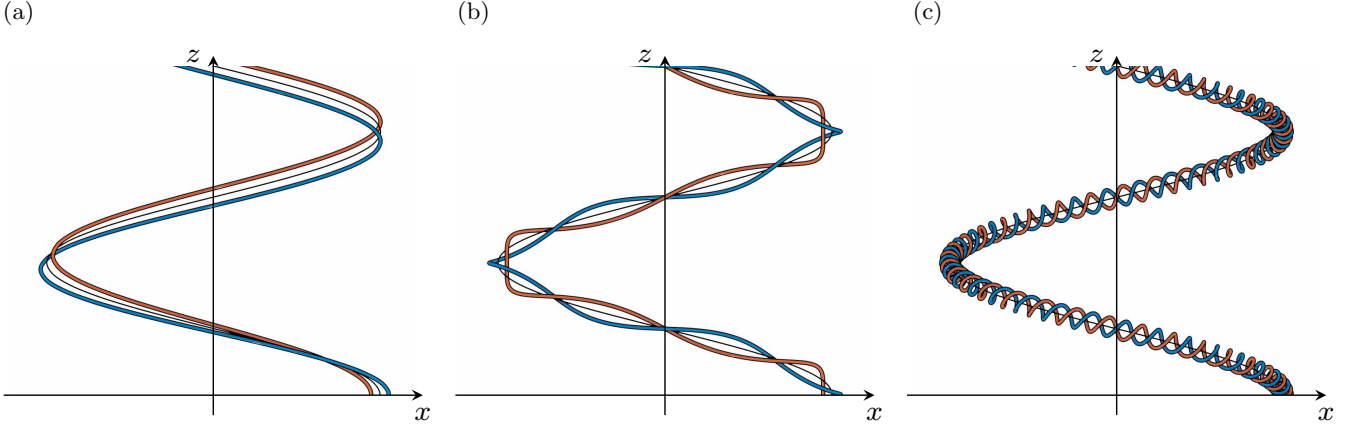


FIG. 2. Geometry described by (6) for $H = 10$, $R = 10$, $d = 1$ and: (a) $h_\tau = 128$ (or $\beta \approx 0.5$); (b) $h_\tau = 32$ (or $\beta \approx 2$); and (c) $h_\tau = 2$ (or $\beta \approx 31.8$).

A. Simplified approach

1. Geometrical parameters

In the present situation, the far-field structure is expected to be close to a double helix inscribed on a “larger” underlying helix. Such idealized structure is defined by the geometric parameters identified in figure 1. The double-helix has a radius $d/2$ and pitch h_τ (corresponding to an axial pitch h) while the large helix, noted \mathcal{H} , has a radius R and axial pitch H . Another important parameter is the ratio $\beta \equiv H/h = 2\pi/\tilde{\theta}$ (see figure 1). Depending on the values of H , R , h_τ , and d , the double-helix structure may describe: (i) a leapfrog-type pattern where vortices trade places every $1/\beta$ turns (figure 2a); (ii) a relatively sparse braid (figure 2b); or (iii) a dense ‘telephone cord’-type pattern (figure 2c). We are typically in situation (i) when $\beta < 1$ and $h_\tau/d > 10$, and in situation (iii) when $h_\tau/d < 5$ and $\beta > 5$.

The curve \mathbf{X}_0 described by \mathcal{H} is defined in a Cartesian frame as a function of the angular coordinate θ_0 by

$$x_0 = R \cos \theta_0 \quad (5a)$$

$$y_0 = R \sin \theta_0 \quad (5b)$$

$$z_0 = H\theta_0/(2\pi) \quad (5c)$$

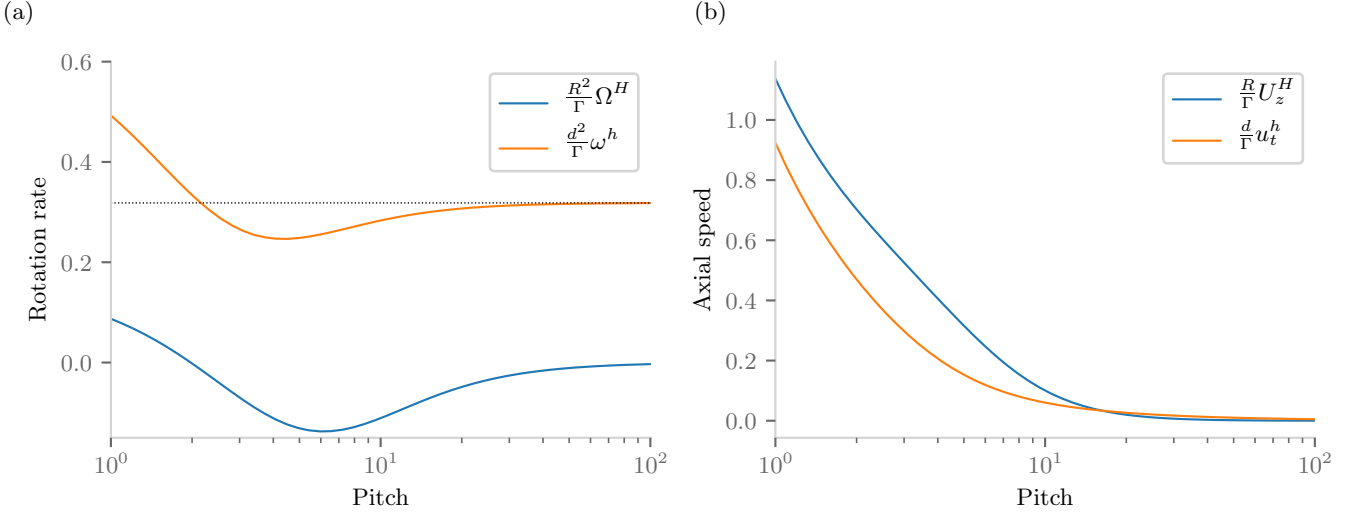


FIG. 3. Dimensionless rotation rate (a) and axial speed (b) of the vortex elements on an helix of radius R , circulation 2Γ and core size $d = 0.1R$ as a function of the dimensionless pitch H/R (in blue) and on a double-helix of radius $d/2$, circulation Γ and core size $a = 0.2d$, as a function of the dimensionless pitch $2h_\tau/d$ (in orange). The dotted line in (a) indicates the value $d^2\omega^h/\Gamma = 1/\pi$.

while the curves \mathbf{X}_i , $i = 1, 2$ described by the double-helix are defined by

$$x_i = x_0 + (d/2) \cos \phi_i \cos \theta_0 - c_\tau (d/2) \sin \phi_i \sin \theta_0 \quad (6a)$$

$$y_i = y_0 + (d/2) \cos \phi_i \sin \theta_0 + c_\tau (d/2) \sin \phi_i \cos \theta_0 \quad (6b)$$

$$z_i = z_0 - c_\kappa (d/2) \sin \phi_i \quad (6c)$$

where $\phi_1 \equiv \beta\theta_0$ and $\phi_2 \equiv \beta\theta_0 + \pi$ define the orientation of the helices relative to the chord plane. The torsion coefficient c_τ and the curvature coefficient c_κ of \mathcal{H} are given by,

$$c_\tau \equiv \frac{|H|}{\sqrt{4\pi^2 R^2 + H^2}}, \quad c_\kappa \equiv \frac{2\pi R}{\sqrt{4\pi^2 R^2 + H^2}}. \quad (7)$$

We also note that h_τ and h are related with each other by the relation

$$h_\tau = \frac{h}{c_\tau}. \quad (8)$$

The above structure satisfies the following form of spatial periodicity: it is invariant by the double operation $z \rightarrow z + h$ and $\theta_0 \rightarrow \theta_0 + \tilde{\theta}$. Moreover, since we consider vortices of equal core size a and circulation Γ , both vortices are deemed as interchangeable, such that our periodic domain is further reduced to a domain of axial length $h/2$ and azimuthal angle $\tilde{\theta}/2$. In the following, we keep this property to obtain the solutions. In particular, we assume that there is a single location in an axial period $h/2$ where both vortices are at the same azimuth. We chose this azimuth to define the radius R and separation distance d . The axial period h then defines a mean axial pitch while H is obtained from $H = 2\pi h/\tilde{\theta}$. In addition to the core size a , these length scales can be used to define four dimensionless parameters

$$R^* \equiv \frac{R}{d}, \quad H^* \equiv \frac{H}{d}, \quad h_\tau^* \equiv \frac{h_\tau}{d}, \quad \varepsilon \equiv \frac{a}{d}, \quad (9)$$

that will characterize our solutions in the far-field.

2. Characteristics of the moving frame

A vortex ring and a helical vortex are examples of vortex structures that move in space at a constant speed without deformation [30]. The double-helix structure is also bound to move by the induction of velocity it generates. For this structure, one can naturally assume that the self-induced velocity would be predominantly composed of:

- a translation of velocity u_t and rotation of angular velocity ω around the double-helix axis, i.e., \mathcal{H} .
- a translation of velocity U_z and rotation of angular velocity Ω around the large helix axis, i.e., the vertical axis.

Under this assumption, we can show there exists a unique frame rotating and translating along the vertical axis where the double-helix geometry shown in figure 1 remains steady. The idea is to use the property that an helix of pitch H is unperturbed by a rotation of angular velocity Ω^a and translation of axial velocity U_z^a provided that

$$U_z^a/\Omega^a = \pm H/(2\pi) \quad (10)$$

where the sign is $+$ for right-handed helices, and $-$ for left-handed helices. The self-rotation of the double-helix can then be cancelled by adding a motion of velocity $u_t^a = \mp h_\tau \omega/(2\pi)$ along the double-helix axis. This motion corresponds to an axial rotation of angular velocity $c_\kappa u_t^a/R$ plus an axial translation of velocity $c_\tau u_t^a$. These velocities add up to the self-induced velocities of the large helix. Both sums can be cancelled if one chooses the frame velocities such that

$$\Omega^F = \Omega + \frac{c_\kappa u_t}{R} \mp \frac{h}{H} \omega, \quad U_z^F = U_z + c_\tau u_t \mp \frac{c_\tau h_\tau}{2\pi} \omega. \quad (11)$$

These expressions will be used as initial guess values for the frame velocity in the numerical procedure described in the next section. If the vortices have a circulation Γ , we shall use

- for the self-induced motion (ω and u_t) of the double-helix, the values obtained by the cut-off method with a Gaussian vortex core of radius a for a straight double helix of circulation Γ and the same geometrical parameters (pitch h_τ , radius $d/2$).
- for the self-induced motion (Ω and U_z) of the large helix \mathcal{H} , the values obtained by the cut-off method with a Gaussian vortex core of “effective” radius $d/2$ for an helix of circulation 2Γ , pitch H and radius R .

Typical values for these velocities are provided as function of the non-dimensional pitch in figure 3. In the following, we shall refer to (11) with these estimates as the rectilinear approximation for the frame velocity.

B. Numerical solutions

In the previous section, a prescribed shape for the solutions has been assumed. This hypothesis will turn out to be too strong. We shall see that the helices must deform to be compatible with the self-induced motion. For the numerical procedure, we use the separation distance d and the vortex circulation Γ to normalize time and length scales. The solutions will then only depend on the four dimensionless parameters R^* , H^* , h_τ^* and ε introduced in (9). To reduce the size of the parameter space, only H^* and h_τ^* will be varied. In most cases, we shall use $R^* = 9.5$ and $\varepsilon = 0.2$.

1. Governing equations in helical coordinates

To describe the far-field, it is useful to introduce a local Serret-Frenet basis ($\hat{\mathbf{e}}_{r0}, \hat{\mathbf{e}}_t, \hat{\mathbf{e}}_b$) based on \mathcal{H} and centered at \mathbf{X}_0 as illustrated in figure 4a. The position vector \mathbf{X}_j will then be defined by its local coordinates $r'_j = (r_j - R^*)$ and b'_j in the local perpendicular basis ($\hat{\mathbf{e}}_{r0}, \hat{\mathbf{e}}_b$), see figure 4b. Developing \mathbf{T}_j in terms of ($\hat{\mathbf{e}}_{r0}, \hat{\mathbf{e}}_t, \hat{\mathbf{e}}_b$), the steadiness condition (3) may be written as

$$\frac{dr'_j}{d\theta_0} = \left(\frac{R^*}{c_\kappa} + c_\kappa r'_j \right) \frac{U_{r0} - U_{r0}^F}{U_t - U_t^F} + c_\tau b'_j, \quad \frac{db'_j}{d\theta_0} = \left(\frac{R^*}{c_\kappa} + c_\kappa r'_j \right) \frac{U_b - U_b^F}{U_t - U_t^F} - c_\tau r'_j \quad (12)$$

Because of the spatial periodicity and interchangeability conditions, the calculation domain is comprised between $\theta_0 = 0$ and $\theta_0 = \theta/2$, with

$$\tilde{\theta} = 2\pi/\beta \quad (13)$$

being the half-period of the vortex pair. Our description is completed by the following boundary conditions

$$\begin{cases} r'_1(0) = r'_2(\tilde{\theta}/2) = +\frac{1}{2}, \\ r'_2(0) = r'_1(\tilde{\theta}/2) = -\frac{1}{2}, \end{cases} \quad \begin{cases} b'_1(0) = b'_2(\tilde{\theta}/2) = 0, \\ b'_2(0) = b'_1(\tilde{\theta}/2) = 0. \end{cases} \quad (14)$$

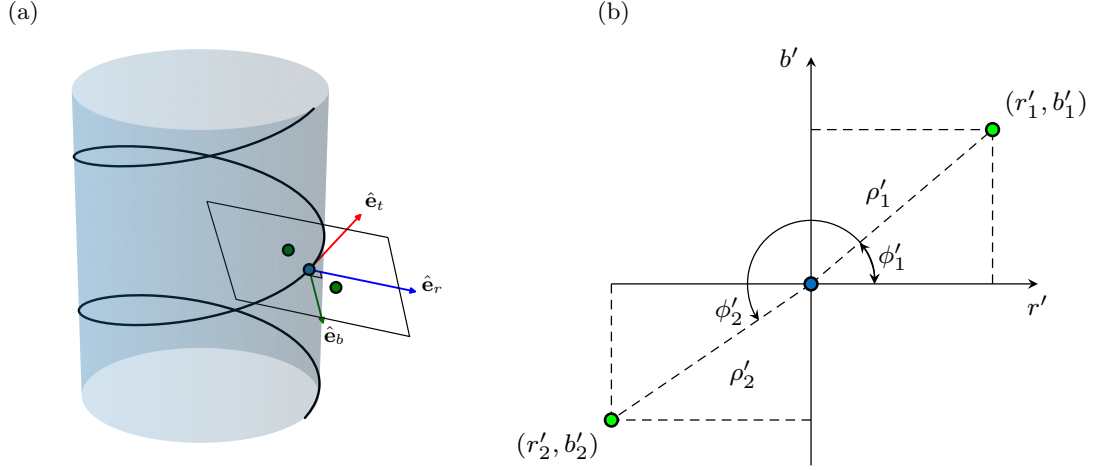


FIG. 4. (a) Local helical basis following \mathcal{H} and (b) 2-D coordinates in the (r', b') plane.

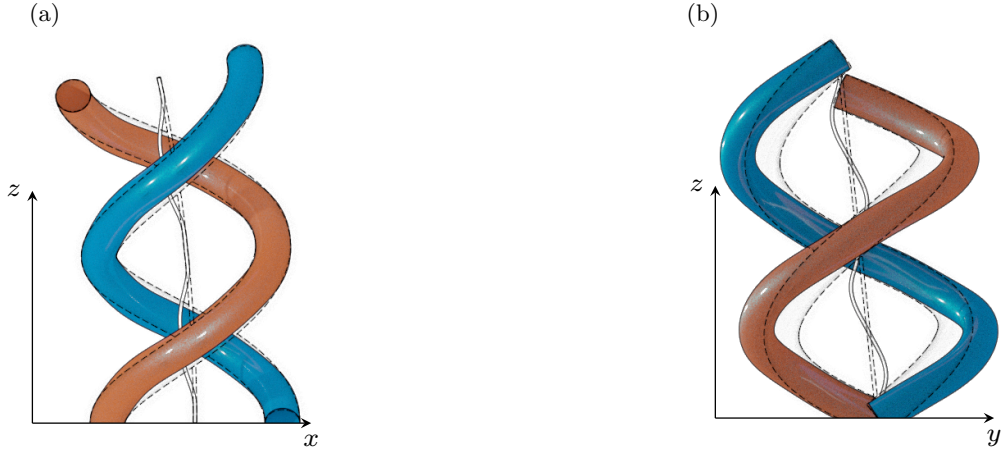


FIG. 5. Close-up of the deformed vortex structure for $H^* = 6.5$ and $h_\tau^* = 2$ over a single period. Numerical solution (in colour) superimposed to the undeformed initial guess (in dashed lines).

Equation (12) is solved numerically as a non-linear minimization problem. Starting from an initial guess for (r'_j, b'_j) obtained from (6)

$$r'_1 = \frac{1}{2} \cos(\beta\theta_0), \quad b'_1 = \frac{1}{2} \sin(\beta\theta_0), \quad r'_2 = \frac{1}{2} \cos(\beta\theta_0 + \pi), \quad b'_2 = \frac{1}{2} \sin(\beta\theta_0 + \pi), \quad (15)$$

and an initial guess for Ω^F and U_z^F obtained from (11), one applies an iterative procedure. At step n of this procedure, one integrates (12) between $\theta_0 = 0$ and $\theta_0 = \tilde{\theta}/2$ to compute the new values of Ω^F and U_z^F which satisfy the boundary conditions. Then, the next iteration of (r'_j, b'_j) is computed from the residual value of (12) using Newton's method. Steps are repeated until the current and subsequent iterations converge. To fix the spatial resolution, we check for grid convergence using the primitive variables, local curvature coefficient, and frame velocities. In practice, for most calculations we use $p_n = 48$ segments per period.

2. Geometry of the solutions

In this section, we characterize the geometry of the solutions, especially their departure from the (undeformed) initial guess. In general, solutions keep the overall form of the approximated solutions, but the helical symmetries are now broken (figures 5a and 5b). Both the double-helix structure and the large underlying helix deform. Some useful

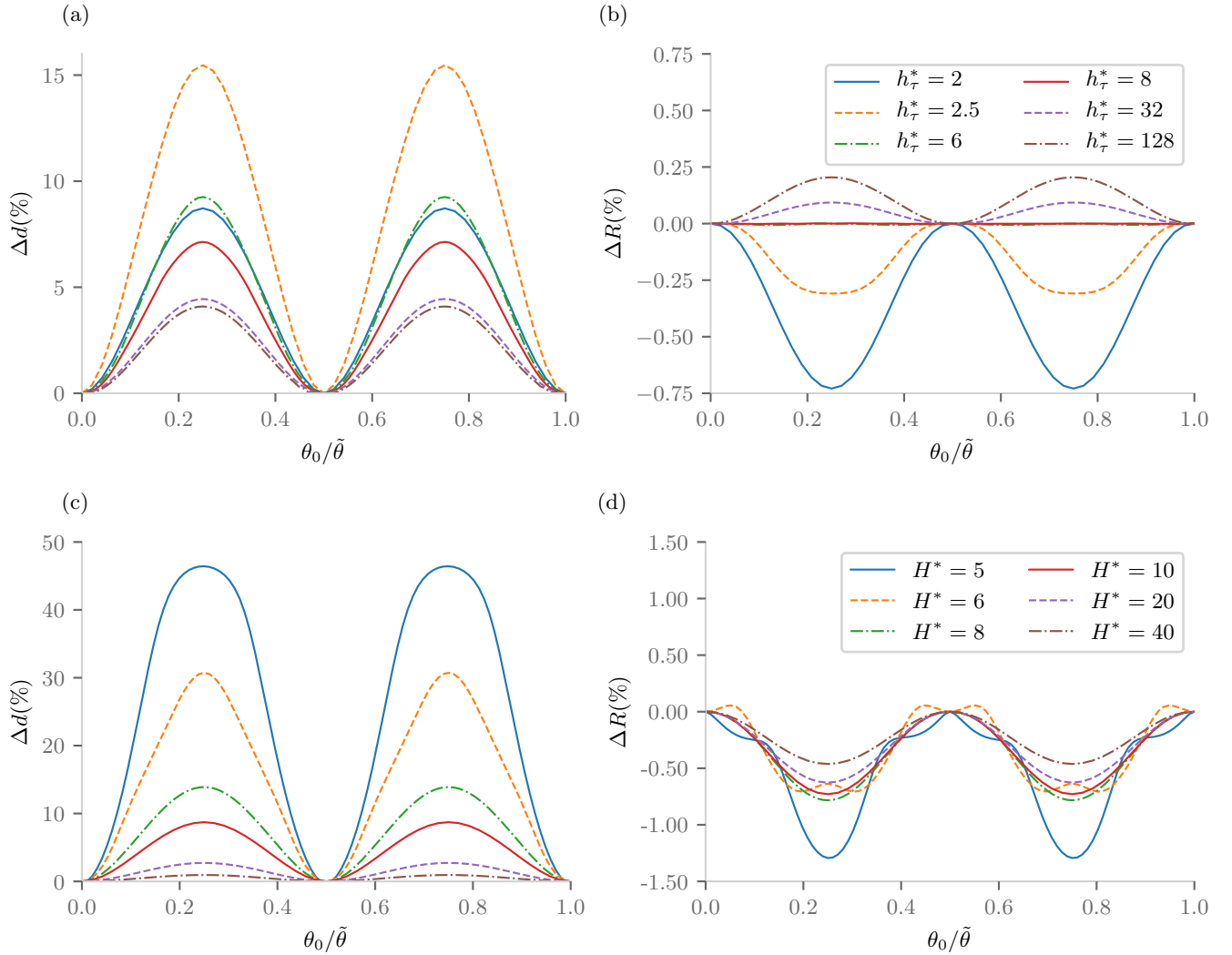


FIG. 6. (a,c) Change in the separation distance Δd and (b,d) mean radius ΔR as function of θ_0 for: (a,b) $H^* = 10$ and different h_τ^* ; and (c,d) $h_\tau^* = 2$ and different H^* .

indicators of this deformation are the relative changes of the separation distance and of the mean radius defined by

$$\Delta d(\theta_0) = \sqrt{(r'_1 - r'_2)^2 + (b'_1 - b'_2)^2} - 1, \quad \Delta R(\theta_0) = \frac{\sqrt{x_1^2 + y_1^2} + \sqrt{x_2^2 + y_2^2}}{2R^*} - 1, \quad (16)$$

respectively. A positive (resp. negative) Δd indicates that the distance between the two vortices is increasing (resp. decreasing). Similarly, a positive (resp. negative) ΔR indicates an increase (resp. decrease) of the mean radius. By construction, $\Delta d(0) = \Delta d(\tilde{\theta}/2) = \Delta R(0) = \Delta R(\tilde{\theta}/2) = 0$. Both quantities are shown to vary over a single period and their evolution varies with the type of solution (figure 6). For instance, Δd remains relatively constant for leapfrogging solutions (see, $h_\tau^* = 32$ and $h_\tau^* = 128$ in figure 6a), increases as the wake becomes sparsely braided ($h_\tau^* = 6$ and $h_\tau^* = 8$), and reaches a plateau for densely coiled wakes ($h_\tau^* = 2$ and $h_\tau^* = 2.5$). Conversely, ΔR is positive for leapfrogging wakes, close to zero for sparsely braided wakes, and negative for densely coiled wakes. For H^* smaller than a critical value ($H^* \approx 7$ in figure 6b), the variations of ΔR change as the minimum in $\tilde{\theta}/4$ becomes a local extremum. The maximum $|\Delta R|$ initially contracts, before increasing once again as H^* decreases, see figure 7b. This coincides with a plateau in Δd , before increasing again as H^* decreases. Below this point, numerical convergence becomes increasingly hard to obtain for this family of solutions.

For applications, it is interesting to compare these solutions to a similar configuration composed of N pairs of vortices of circulation Γ . In this context, this wake geometry would represent the far-field in a Joukowski rotor wake model [31], but produced by a N -bladed tip-splitting rotor. Figure 8a (resp. 8b) displays the wake geometry obtained

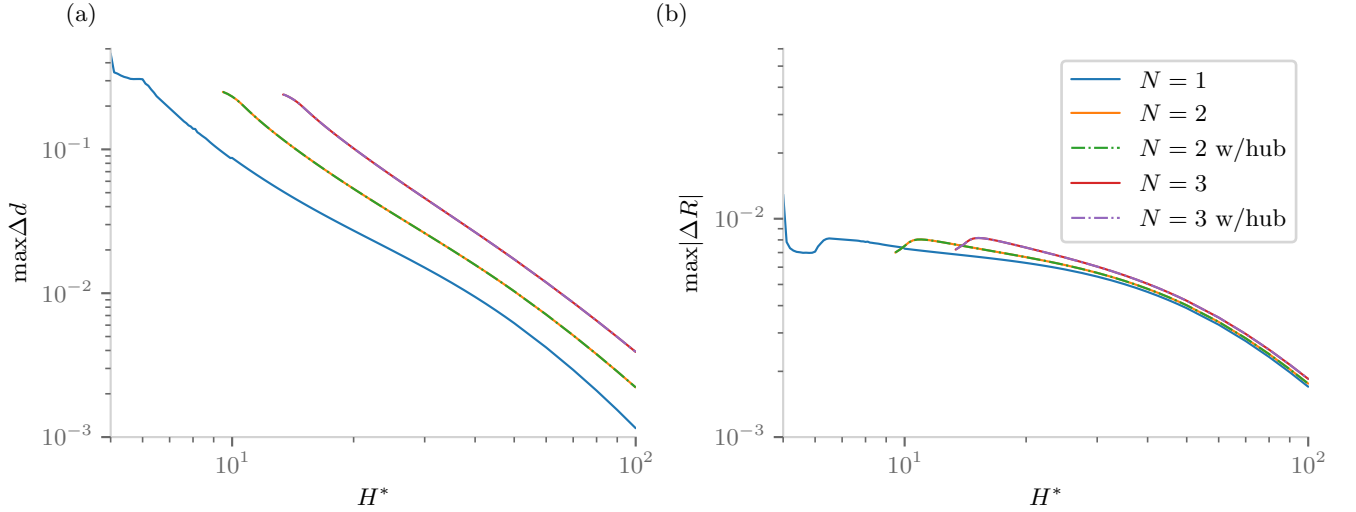


FIG. 7. Maximum change in (a) the separation distance Δd and (b) mean radius $|\Delta R|$ as function of H^* for $h_\tau^* = 2$ and N vortex pairs with and without a straight hub vortex of circulation $-2N\Gamma$.

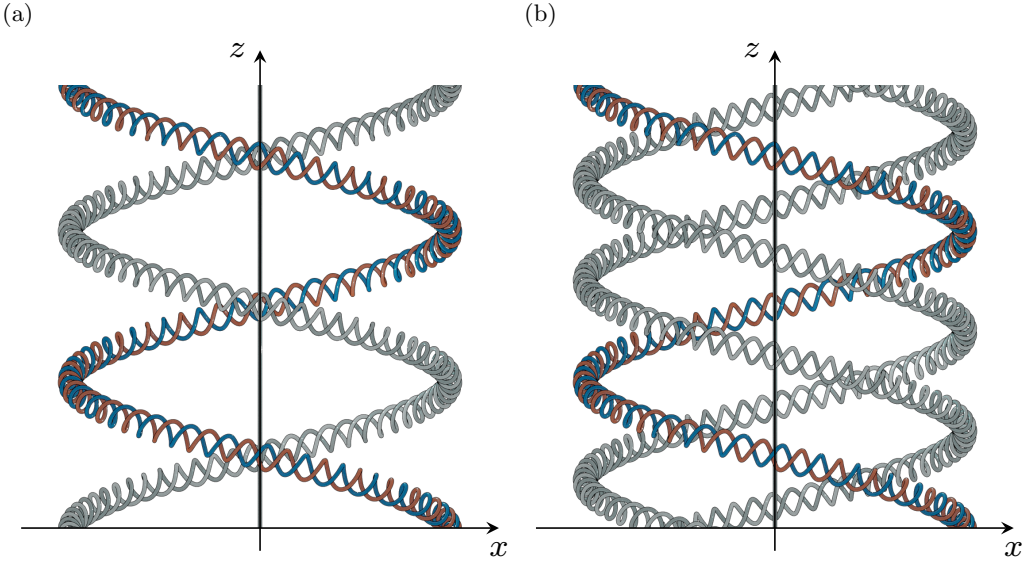


FIG. 8. Deformed structures for (a) two vortex pairs and (b) three vortex pairs including a straight hub vortex of circulation $-2N\Gamma$ for $H^* = 15$ and $h_\tau^* = 2$.

for two (resp. three) vortex pairs for $h_\tau^* = 2$. In general, for equal (H^*, h_τ^*) , deviations from (6) are found to increase with N (figure 7). However, if we base our comparison on the separating distance between neighbouring spires, the deformation actually decreases with N . A similar effect has been reported for counter-rotating helical vortices [15]. Finally, we note that including a straight vortex hub of circulation $-2N\Gamma$ was shown to have little effect on the wake geometry. Unless otherwise stated, in the sequel, we shall focus on the case for $N = 1$ without a hub vortex.

3. Frame and tangential velocities

The numerical procedure provides the frame velocities Ω^F and U_z^F where the structure is steady. These quantities are plotted as a function of h_τ^* (resp. H^*) in figure 9 (resp. figure 10). They are compared to the rectilinear approximation obtained in §III A 2 (in dash-dotted lines) and to a first order approximation obtained by numerically computing the frame velocities with an undeformed solution (in dashed lines). Both approximations work well for

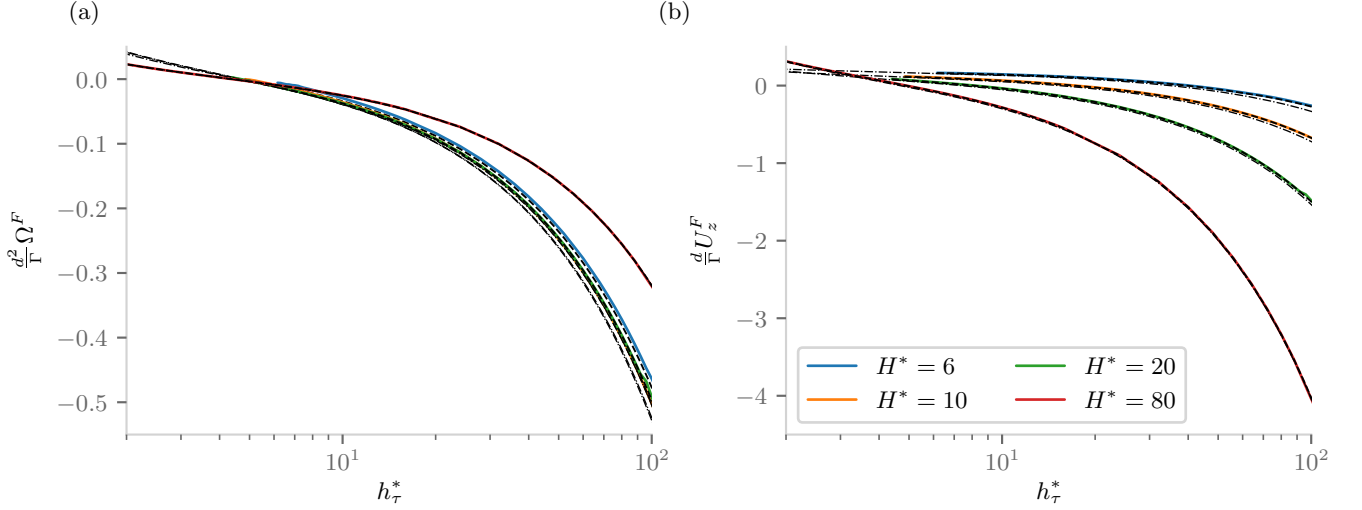


FIG. 9. Frame velocities as function of h_τ^* . Numerical solutions (in solid lines) are compared to the rectilinear approximation (in dash-dotted lines) and to a first order approximation based on the undeformed initial guess (in dashed lines).

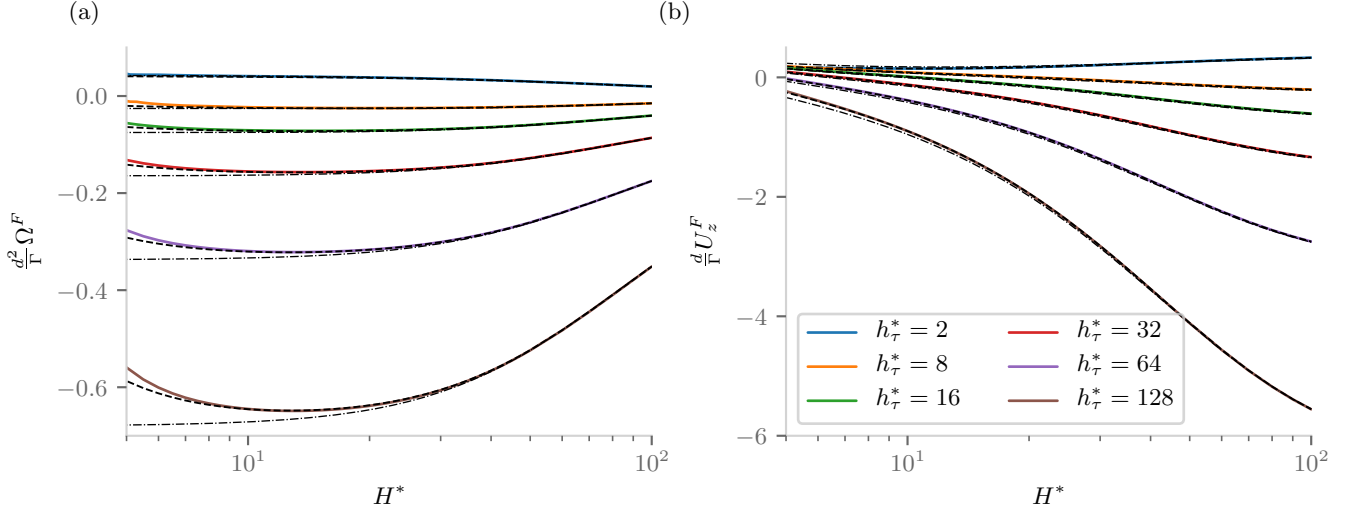


FIG. 10. Frame velocities as function of H^* . Numerical solutions (in solid lines) are compared to the rectilinear approximation (in dash-dotted lines) and to a first order approximation based on the undeformed initial guess (in dashed lines).

large H^* and large h_τ^* , when self-induction is expected to be small. The first order approximation, which takes into account the mutual- and self-induced velocities but neglects the deformation, is naturally better and provides accurate estimates whenever the deformations are weak.

Now let us consider the velocities relative to the moving frame. By construction, the vortex elements are advected along the stationary vortex structure, where $U_{tan} > 0$ indicates an advection in the positive axial direction and *vice versa*. In general, values of U_{tan} are positive (resp. negative) for $h_\tau^* < 0$ (resp. $h_\tau^* > 0$). The tangential velocity varies with respect to θ_0 identically for the internal and external vortices but is shifted by a half-period. Variations are generally small with respect to mean velocity \bar{U}_{tan} . As seen on figures 11a and 11b, \bar{U}_{tan} displays a linear dependency on h_τ with only a weak dependency on H^* for $H^* < 10$. Figure 11a also shows that whatever h_τ^* and H^* the main contribution to the tangential velocity is the translation speed U_t along the large helix. We suspect that this comes from the large value of R^* that we have considered ($R^* = 9.5$).

It is also interesting to compare U_t to the velocity associated with the moving frame

$$U_t^F = c_\tau U_z^F + c_\kappa R^* \Omega^F \quad (17)$$

since the difference between the two is issued from vortex induction. For weakly braided configurations ($h_\tau^* > 10$),

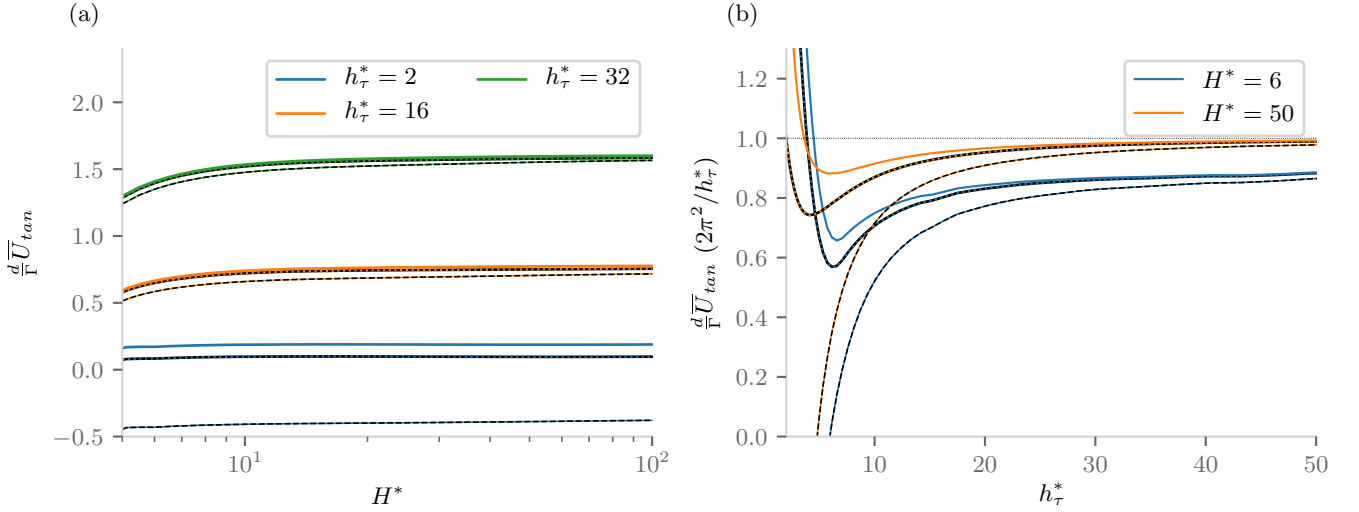


FIG. 11. Evolution of \bar{U}_{tan} (in solid lines) and \bar{U}_t (in dotted lines) as function of (a) H^* and (b) h_τ^* . Numerical solutions are also compared to the velocity associated with the moving frame \bar{U}_t^F (in dashed lines).

most of the tangential velocity is associated with the moving frame and the role of vortex induction is generally small. Note in particular that when H^* is also large, we recover the estimate $\bar{U}_{tan} \approx h_\tau \Gamma / (2\pi^2 d^2)$ obtained from the rectilinear approximation in this limit. By contrast, for densely coiled wakes, such as $h_\tau^* = 2$, \bar{U}_{tan} and \bar{U}_t can be significantly larger than \bar{U}_t^F and even point opposite directions (figure 11b).

4. Properties of the induced flow

For applications, it is useful to know the velocity field induced by the vortex structure. In this section, the induced flow is provided in cross planes and compared to the predictions obtained for perfect helices [32]. Figures 12a-c show the axial and angular velocity components taken at the plane $z = 0$ (where both vortices have the same azimuth) for a leapfrogging, sparsely braided and densely coiled structures, respectively. In these plots, we subtract the frame velocities such that the velocity field vanishes far from the center. Vortex cores intersect the plane on numerous occasions resulting in inhomogeneous velocity and vorticity distributions. For densely coiled structures, this results in regions of very intense angular velocity and opposite signed vorticity. Nevertheless, away from the vortex cores the induced velocity is reminiscent to that of a helical vortex.

To highlight this similarity, consider the azimuthally averaged velocity profiles presented in figure 13a. Inside the region $R^* - 1/2 < r < R^* + 1/2$, the angular velocity displays a maximum around $r = R^*$, while the axial velocity can be roughly approximated by a linear function. Outside the region $R^* - 1/2 < r < R^* + 1/2$, the azimuthally averaged profiles approach the ideal profiles of a uniform helix [32]

$$\langle U_z^H \rangle_\theta = \begin{cases} 2\Gamma/H & \text{if } r < R^* - 1/2 \\ 0 & \text{if } r > R^* + 1/2 \end{cases}; \quad \langle \Omega^H \rangle_\theta = \begin{cases} 0 & \text{if } r < R^* - 1/2 \\ \Gamma/(\pi r^2) & \text{if } r > R^* + 1/2 \end{cases}. \quad (18)$$

where $R_{tip} = R^* + 1/2$ and $R_{vane} = R^* - 1/2$.

Close to the vortex cores, the velocity field can be better understood by projecting the velocity components into the local helical frame (ρ', ϕ') , where the velocity field is consistent with a double-helix locally aligned with \mathcal{H} . This is shown in figure 13b, where the ϕ' -averaged profiles also approach the mean profiles of a perfect double helix

$$\langle U_t^h \rangle_{\phi'} = \begin{cases} 2\Gamma/h_\tau & \text{if } \rho' < (1 - \varepsilon)/2 \\ 0 & \text{if } \rho' > (1 + \varepsilon)/2 \end{cases}; \quad \langle \omega^h \rangle_{\phi'} = \begin{cases} 0 & \text{if } \rho' < (1 - \varepsilon)/2 \\ \Gamma/(\pi \rho'^2) & \text{if } \rho' > (1 + \varepsilon)/2 \end{cases}. \quad (19)$$

The above results highlight the dual nature exhibited by this vortex structure. Solutions for closely spaced co-rotating helical vortices issue from a balance between contributions at different scales with long-distance effects primarily governed by the large-scale helix and more local features defined by the double-helix geometry.

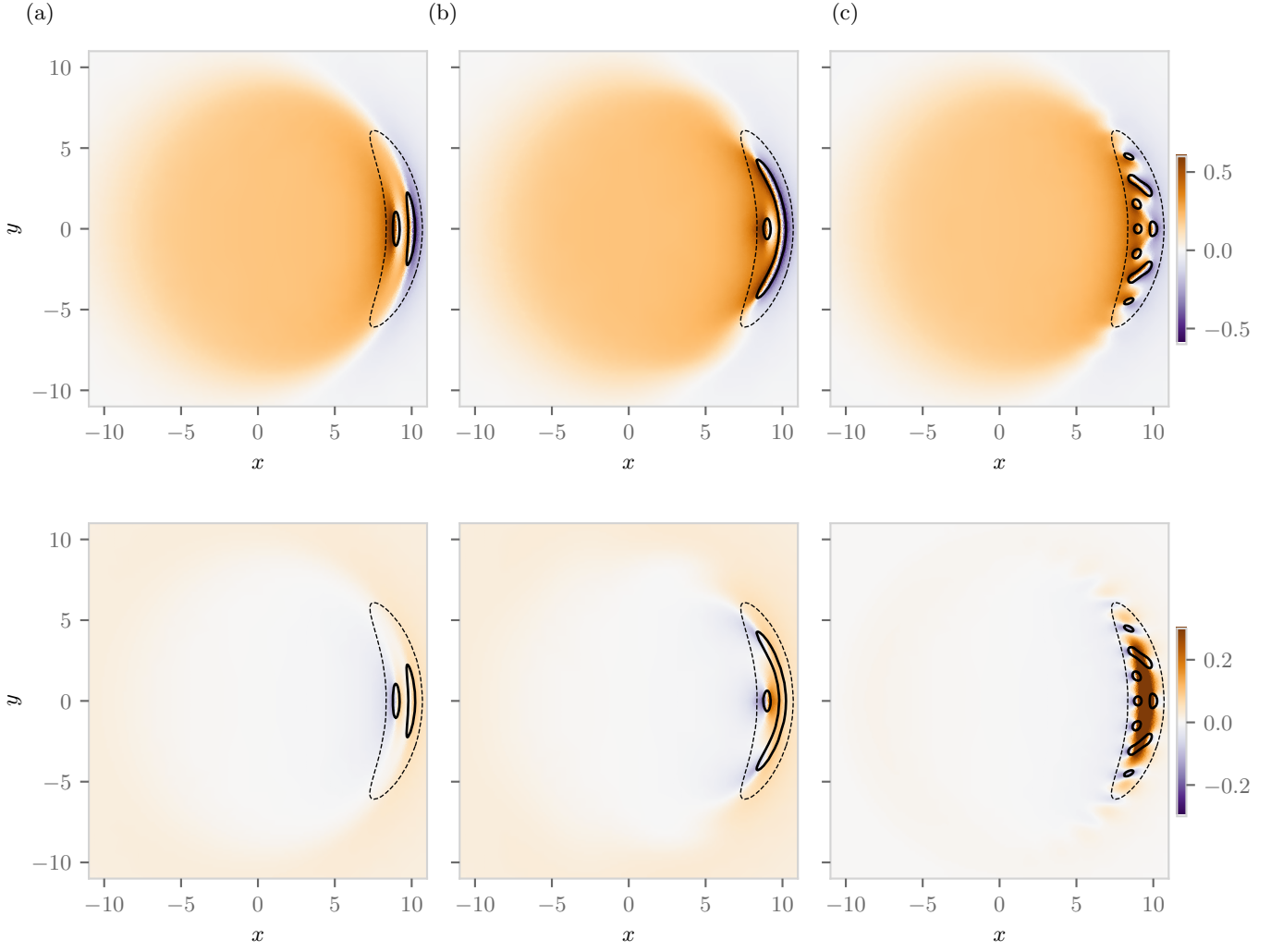


FIG. 12. Axial velocity $\frac{d}{dt}U_z$ (top) and angular velocity $\frac{d}{dt}U_\theta$ at the plane $(x, y, z) = 0$ for $H^* = 10$. (a) Leapfrogging wake for $\beta = 1$, (b) sparsely braided wake for $\beta = 4$, and (c) densely coiled wake for $\beta = 16$. Solid lines indicate the intersection with the vortex cores, while dashed lines correspond to a helical vortex tube enclosing the twin-vortex.

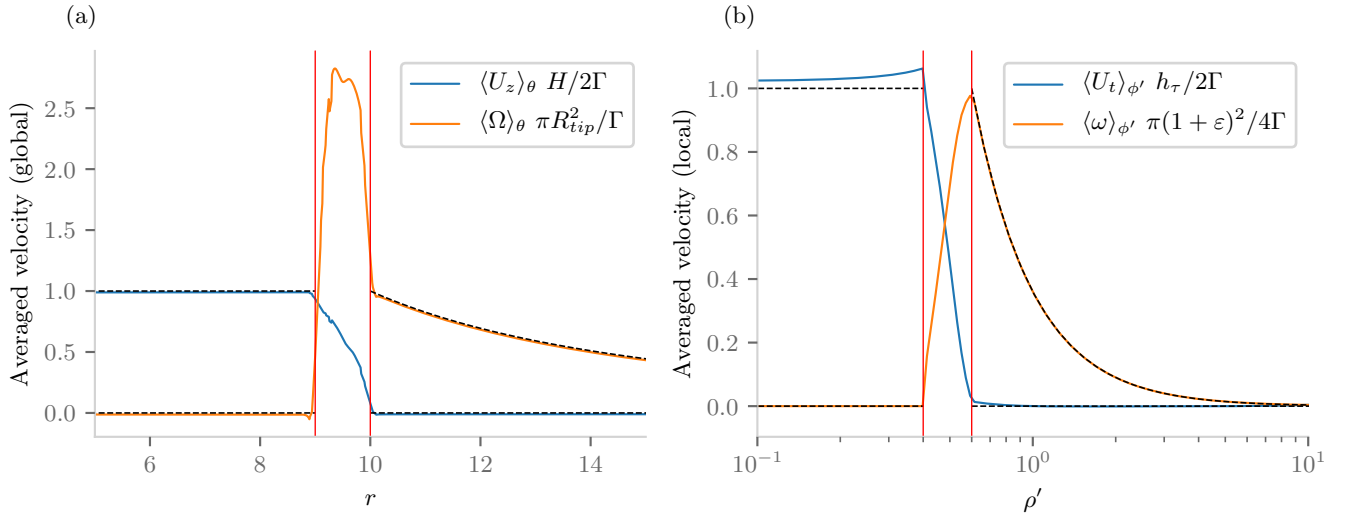


FIG. 13. Azimuthally averaged velocity profiles for $H^* = 10$ and $h_\tau^* = 2$. Fig. (a) (resp. (b)) Rotation rate and axial velocity component in the global cylindrical (resp. local helical) frame. Dashed lines correspond to expressions (18) (resp. (19)).

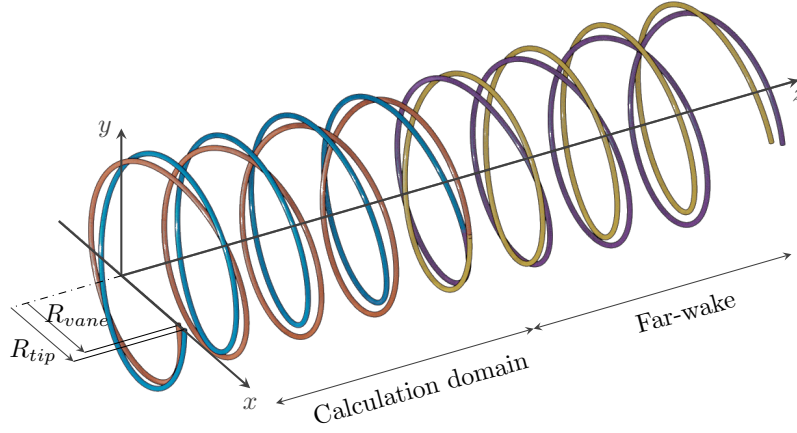


FIG. 14. Schematic representation of the semi-infinite case: two co-rotating vortices are emitted from a rotor blade at radial positions R_{vane} and R_{tip} , respectively. The calculation domain and the prescribed far-wake are shown in different colors.

IV. NEAR-FIELD SOLUTIONS

In the previous section, we have described the solutions in the far-field. In this section, we consider the vortex structure close to the rotor plane. The objective is not to perform a complete parametric study but to illustrate how these solutions can describe the wake of a tip-splitting rotor under different flight regimes.

A. Numerical method

There is one notable difference with respect to the analysis performed in the previous section. Instead of fixing the geometric parameters to find the associated frame velocities, now we solve the inverse problem. That is, we fix the operating conditions - the rotation rate $\Omega^F = \Omega_R$ and external velocity $U_z^F = -U_\infty$, and compute the corresponding wake geometry. Now the prescribed geometrical parameters are the radial coordinates $r = R_{vane} = R_0 - d_0/2$ and $r = R_{tip} = R_0 + d_0/2$ where the vortices are emitted on the rotor blade (located at $\theta_0 = 0$ and $z = 0$), and the vortex core size a . As previously, we define four non-dimensional parameters

$$\lambda \equiv \frac{R_0 \Omega_R}{U_\infty}, \quad \eta \equiv \frac{\Gamma}{R_0^2 \Omega_R}, \quad R_0^* \equiv \frac{R_0}{d_0}, \quad \varepsilon_0^* \equiv \frac{a}{d_0}, \quad (20)$$

where λ is known as the tip-speed ratio and η represents the relative vortex strength. As in [15], we choose a convention such that η remains positive, while λ may change sign. Wind turbine regimes will always correspond to positive values of λ . By contrast, helicopters may correspond to either negative values of λ in climbing flight or positive values of λ in descending flight. In the present study, only the parameters η and λ are varied. In most cases, ε_0^* and R_0^* are fixed to 0.2 and 9.5, respectively. Note that these parameters are different from the parameters R^* and ε^* defined above for the far-field, as the mean radius and the vortex separation distance in the far-field are now the results of the calculation.

The near-field solution satisfies (4) with the boundary condition at $\zeta = 0$: $r_1 = R_0 - d_0/2$ and $r_2 = R_0 + d_0/2$ and $\theta_j = z_j = 0$. As we go away from the rotor, it should match a far-field solution. To implement this condition, we follow the numerical procedure used by Durán Venegas *et al.* [15] for Joukowski's rotor wake model. We decompose the induced velocity into contributions from the near-field and far-field. Contributions from the far-field are modeled by imposing that after a certain distance from the rotor plane, the wake adopts the geometry of a far-field solution, see figure 14. The geometrical parameters of this far-wake solution are estimated from the near-field solution at the end of calculation domain. The computational domain must be large enough for the wake to develop and match the far-field. In practice, the size of the domain and of the corresponding far-wake range from 30π to 60π .

B. Description of the steady solutions

Figure 15 displays the wake structure with the corresponding radial coordinates as function of the axial coordinate z . Figure 15a (resp. 15b) is representative of the wind turbine (resp. helicopter) regime, which displays a radial expansion

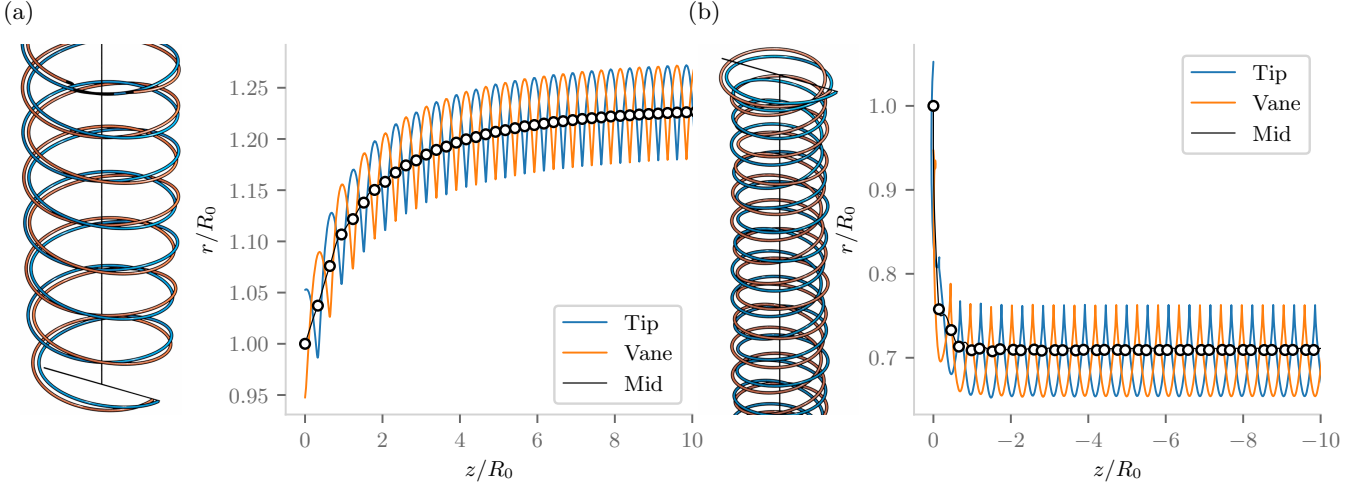


FIG. 15. Schematic representation of the vortex wake and evolution of the radial coordinates r_j as function of z for $\eta = 0.04$, $R_0^* = 9.5$, $\varepsilon_0^* = 0.2$. (a) $\lambda = 5.5$ in a wind turbine regime; (b) $\lambda = 40$ in a helicopter descending flight regime. Markers indicate the positions where both vortices have the same azimuth.

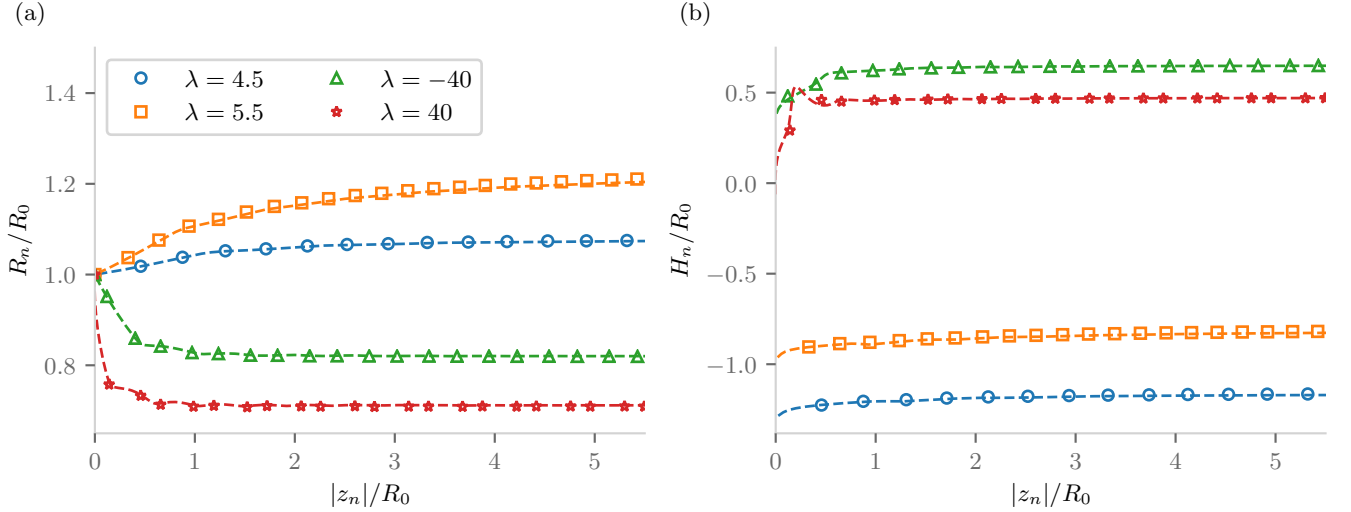


FIG. 16. Evolution of (a) R_n/R_0 , and (b) H_n/R_0 as function of $|z_n|/R_0$ for different values of λ for $\eta = 0.04$, $R_0^* = 9.5$, $\varepsilon_0^* = 0.2$. For each case, we display the corresponding evolution obtained for an ‘equivalent’ helical vortex in dashed lines.

(resp. contraction), while the two vortices trade places continuously. Simultaneously, the separation distance may also contract or expand due to the combined effects of the vortex pair and the rotor’s presence. Additionally, the structure may exhibit local variations of both axial pitches. For clarity, we characterize the wake in terms of the geometric parameters introduced in §III.

1. Evolution of the wake in the near-field

As in §III, we introduce the curve $\mathbf{X}_{mid}(\zeta)$ equidistant to both vortices and the separation distance $d(\zeta)$ defined by

$$\mathbf{X}_{mid}(\zeta) = (\mathbf{X}_{tip}(\zeta) + \mathbf{X}_{vane}(\zeta))/2, \quad (21)$$

$$d(\zeta) = \|\mathbf{X}_{tip}(\zeta) - \mathbf{X}_{vane}(\zeta)\|. \quad (22)$$

We also perform a series of discrete measurements at the points along the curve $(\zeta_n, n = 1, 2, \dots)$ where the internal and external vortices have the same azimuth (indicated by solid marks in figure 15). In this way, the large helix \mathcal{H}

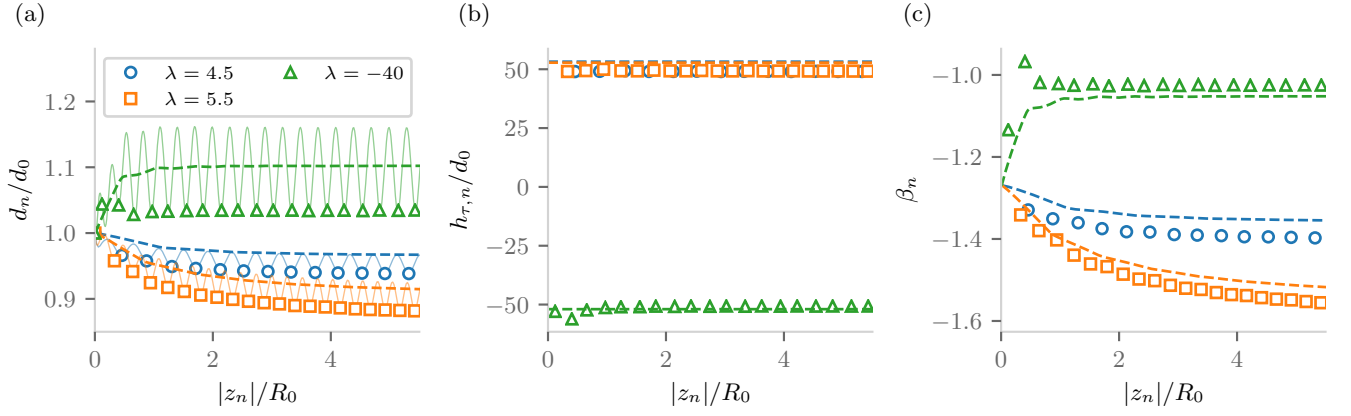


FIG. 17. Evolution of (a) d_n/d_0 , (b) $h_{\tau,n}/d_0$ and β_n as a function of z_n/R_0 for the cases displayed in figure 16. Dashed lines in figures (a) and (b), correspond to (28) and (29), respectively. For reference, the evolution of $d(z)/d_0$ is shown in solid lines in fig. (a).

is characterized by a set of radii and pitches

$$R_n \equiv r_{mid}(\zeta_n), \quad H_n \equiv \frac{z_{mid}(\zeta_{n+1}) - z_{mid}(\zeta_n)}{\theta_{mid}(\zeta_{n+1}) - \theta_{mid}(\zeta_n)}, \quad \text{for } n = 0, 1, 2, \dots \quad (23)$$

which converge towards the values at the far-field R_∞ and H_∞ , respectively.

Figure 16a displays the evolution of R_n/R_0 as a function of $z(\zeta_n)/R_0$ for cases representative of wind turbine and helicopter regimes. Far-field solutions suggest that \mathcal{H} can be modeled by a single tip vortex of circulation 2Γ and core size d emitted from the radial coordinate R_0 under the same operating conditions. A good agreement is observed, between the evolution of R_n/R_0 and the equivalent helix approximation. A similar agreement is observed between H_n/R_0 and the ‘equivalent’ pitch in figure 16b.

Conversely, the rotation of the vortex pair is characterized by a set of mean separation distances and axial pitches

$$d_n \equiv d(\zeta_n), \quad h_n \equiv \frac{z_{mid}(\zeta_{n+1}) - z_{mid}(\zeta_n)}{\pi}, \quad \text{for } n = 0, 1, 2, \dots \quad (24)$$

which converge towards the values at the far-field d_∞ and h_∞ , respectively. Combining both sets of measurements, we obtain a set for the mean pitch and twist parameter

$$h_{\tau,n} \equiv h_n \frac{\sqrt{H_n^2 + 4\pi^2 R_n^2}}{H_n}, \quad \beta_n \equiv \frac{H_n}{h_n}, \quad \text{for } n = 1, 2, \dots \quad (25)$$

which converge towards the values at the far-field $h_{\tau,\infty}$ and β_∞ .

The evolution of these parameters is shown in figures 17a-c. The first remarkable feature is a dynamical similarity between local parameters’ evolution and those of the large helix. Variations are limited to the very near wake, and are rapid whenever those of the large helix are rapid. However, variations seem to be opposite for the small and the large helix: the separation distance d_n increases (resp. decreases) when the large helix radius R_n decreases (resp. increases). The local pitch $h_{\tau,n}$ is also found to have an opposite sign to H_n , meaning that the small and large helices are oriented differently. Additionally, both pitches remain constant in the wake. It is also important to note the large absolute value of $h_{\tau,n}/d_0$, indicating that configurations are weakly twisted where self-induced effects are generally small. This has some consequences that can be used to derive a model explaining the variations of the local properties.

The evolution of the separation distance d_n can be understood by the following arguments. As the radius R_n of the large helix varies, we expect variations of the advection speed U_t of the vortices along \mathcal{H} . These variations are responsible of a local strain that tends to contract the vortex structure (that is, decrease d) when U_t increases, and expand it when U_t decreases. The variations of d are then obtained by the conservation of the mass flux in the vortex stream tube which prescribes that

$$U_t(\zeta_n) d^2(\zeta_n) = cst. \quad (26)$$

An estimate for $U_t(\zeta_n)$ can be obtained when the self-induction is weak. We have seen in §III that in that case, $U_t(\zeta_n)$ is mainly provided by the frame velocity $U_t^F(\zeta_n) = \pm(U_\infty^2 + R_n^2 \Omega_R^2)^{1/2}$ where the \pm sign is defined by the sign

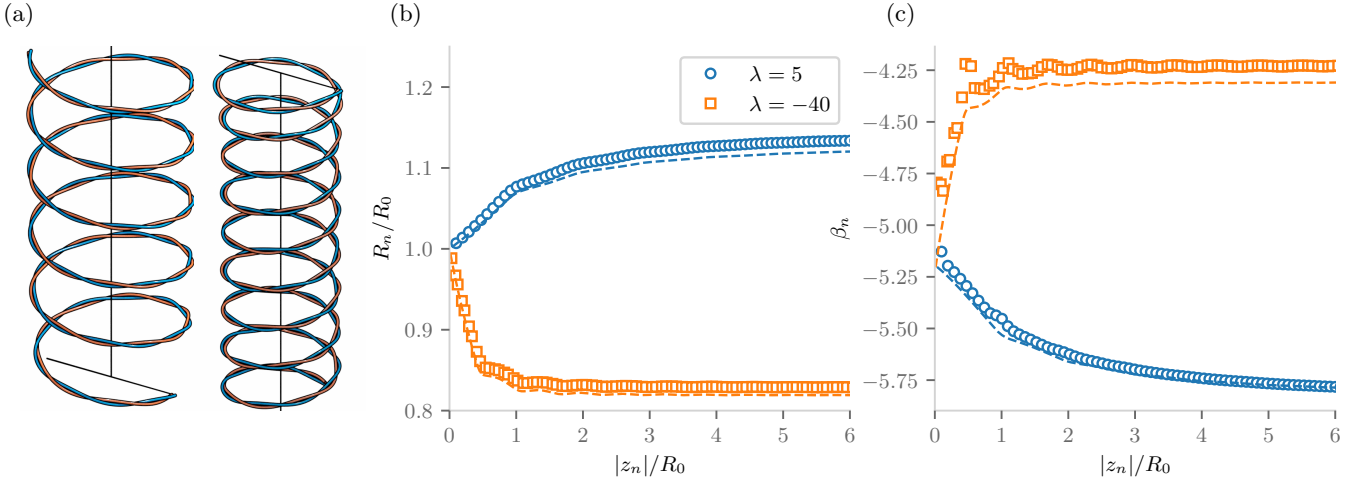


FIG. 18. (a) Sparsely braided wakes obtained for $\eta = 0.04$, $R_0^* = 19.5$, $\varepsilon_0^* = 0.2$ in a wind turbine regime ($\lambda = 5$) and a helicopter climbing flight regime ($\lambda = -40$). (b,c) Evolution of R_n/R_0 and β_n compared to the equivalent helix approximation in dashed lines.

of U_∞ . In terms of the non-dimensionalized parameters λ and η , this gives

$$U_t(\zeta_n) \frac{R_0}{\Gamma} \approx \frac{\sqrt{1 + \lambda^2 R_n^2 / R_0^2}}{\eta \lambda} \quad (27)$$

Combining this expression with (26), we obtain the following relation between d_n and R_n

$$\frac{d_n}{d_0} = \left[\frac{1 + \lambda^2}{1 + \lambda^2 R_n^2 / R_0^2} \right]^{1/4} \quad (28)$$

This expression is tested in figure 17a, where a contraction (resp. expansion) of the separation distance is observed for the wind turbine (resp. helicopter) regimes. While equation (28) gives correct trends and orders of magnitude, it tends to overestimate the expansion and underestimate the contraction. This difference could be explained in different ways. First, the contributions from the double-helix to U_t estimated at the far-field from (19) as $2R_0^* d_0 / h_{\tau,n}$ have been neglected in (27) since vortex induction is rather weak. Second, a radial contraction of the double-helix close to the blade that should also be present but that has not been taken into account. Such contraction could be estimated by analogy to a vortex pair under a locally axial flow U_t . Considering these two effects, would give an additional contraction as observed in the numerics, but still would be too small to account for the discrepancy. Another possibility is the differential expansion/contraction experienced by the two vortices close to the rotor plane due to their radial position. The outermost vortex would experience a larger expansion/contraction than the innermost vortex, thus changing the separation distance. However, since the two vortices continuously trade places with one another, this effect is hard to quantify.

In a similar vein, the pitch of the double-helix can be estimated using $h_\tau = 2\pi U_t / \omega$ where ω is the rotation rate of the vortex pair. As shown in figure 3, for large values of h_τ / d we can approximate ω as $\omega = \Gamma / \pi d^2$. Combining both expressions shows that $h_{\tau,n}$ should be constant and given by

$$\frac{h_{\tau,n}}{d_0} \approx \frac{2\pi^2}{\eta R_0^*} \left[\frac{\sqrt{1 + \lambda^2}}{\lambda} \right] \quad (29)$$

which is verified in figure 17b. Equation (29) also suggests that $h_{\tau,n} / d_0$ is primarily governed by R_0^* and η , since the part shown in brackets remains close to 1 (in absolute value). The condition $h_{\tau,n} / d_0 > 10$ for being weakly twisted then reduces to $\eta R_0^* \lesssim 2$. For $\eta = 0.04$, this condition is satisfied as soon as $R_0^* \lesssim 50$.

From (29), we can also compute the twist parameter $\beta_n = H_n / (h_{\tau,n} c_\tau(\zeta_n))$ as

$$\beta_n \approx -\frac{\eta (R_0^*)^2}{\pi} \left[\frac{|\lambda|}{\sqrt{1 + \lambda^2}} \frac{\sqrt{H_n^2 + 4\pi^2 R_n^2}}{2\pi R_0} \right]. \quad (30)$$

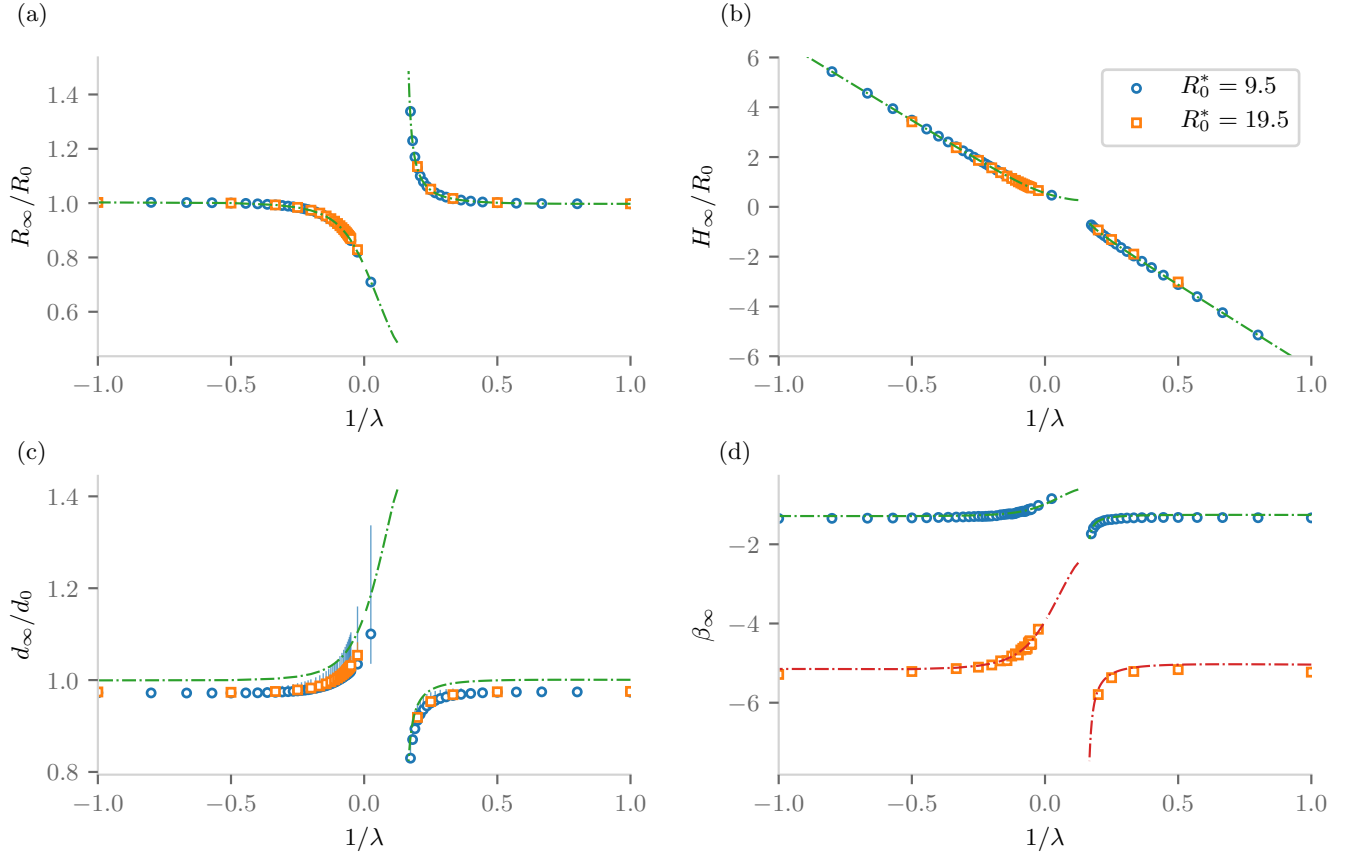


FIG. 19. Evolution of the far-wake parameters as a function of $1/\lambda$ for $\eta = 0.04$, $\varepsilon_0^* = 0.2$. Dashed lines correspond to the equivalent vortex approximations in (a,b) and to equations (29) and (30) in (c,d). For reference, fig. (c) also displays the minimum and maximum values of $d(\zeta)/d_0$ for $\zeta \rightarrow \infty$ as a vertical bar. Helicopter regimes are on the left, wind turbine regimes on the right.

which has been compared to the data in figure 17c. As the part shown in brackets remains in general close to 1, the typical order of $|\beta|$ is then given by the product $\eta(R_0^*)^2$. In particular, we expect to be in a leapfrogging situation ($|\beta| < 1$) as soon as $\eta(R_0^*)^2 \gtrsim \pi$. Equation (30) suggests a simple way to control the twist parameter by increasing R_0^* (i.e. reducing the separation distance d_0). In order to illustrate this point, we consider the same values of (λ, η) for $R_0^* = 19.5$ in different flight regimes and measure β_n . As expected, the evolution of the large-scale pattern is comparable to the equivalent single tip rotor, while β_n is roughly four times larger with respect to the case with $R_0^* = 9.5$ (compare figure 17c and figure 18c).

The above approximations can also be used to predict the characteristics of the far-wake. In figures 19 and 20, we have compared the model with the numerics as both λ and η vary. We can observe in figures 19a,b and 20a,b that for the radius R_∞ and the pitch H_∞ , the agreement with the equivalent vortex approximation is excellent for all regimes. For the separation distance d_∞ (figures 19c and 20c), the trend is qualitatively good but there is a constant systematic over-estimation in the model, that has already been noticed above. The fact that d_∞ changes little with R_0^* is also consistent with (29). Interestingly, the twist parameter β_∞ (figures 19d and 20d) is always found to be well-predicted, probably because it does not directly depend on the separation distance.

V. SUMMARY AND CONCLUSION

In this article, we have obtained using a cut-off filament approach numerical solutions describing the wake generated by a single-bladed tip-splitting rotor. Both infinite solutions describing the far-wake and semi-infinite solutions describing the vortex structure close to rotor plane have been provided. These solutions are stationary in the frame rotating with the rotor blade. We have shown that they can be understood as a double helix motion on a larger helical structure. This interpretation has allowed us to derive a simple model that captures the main features of the

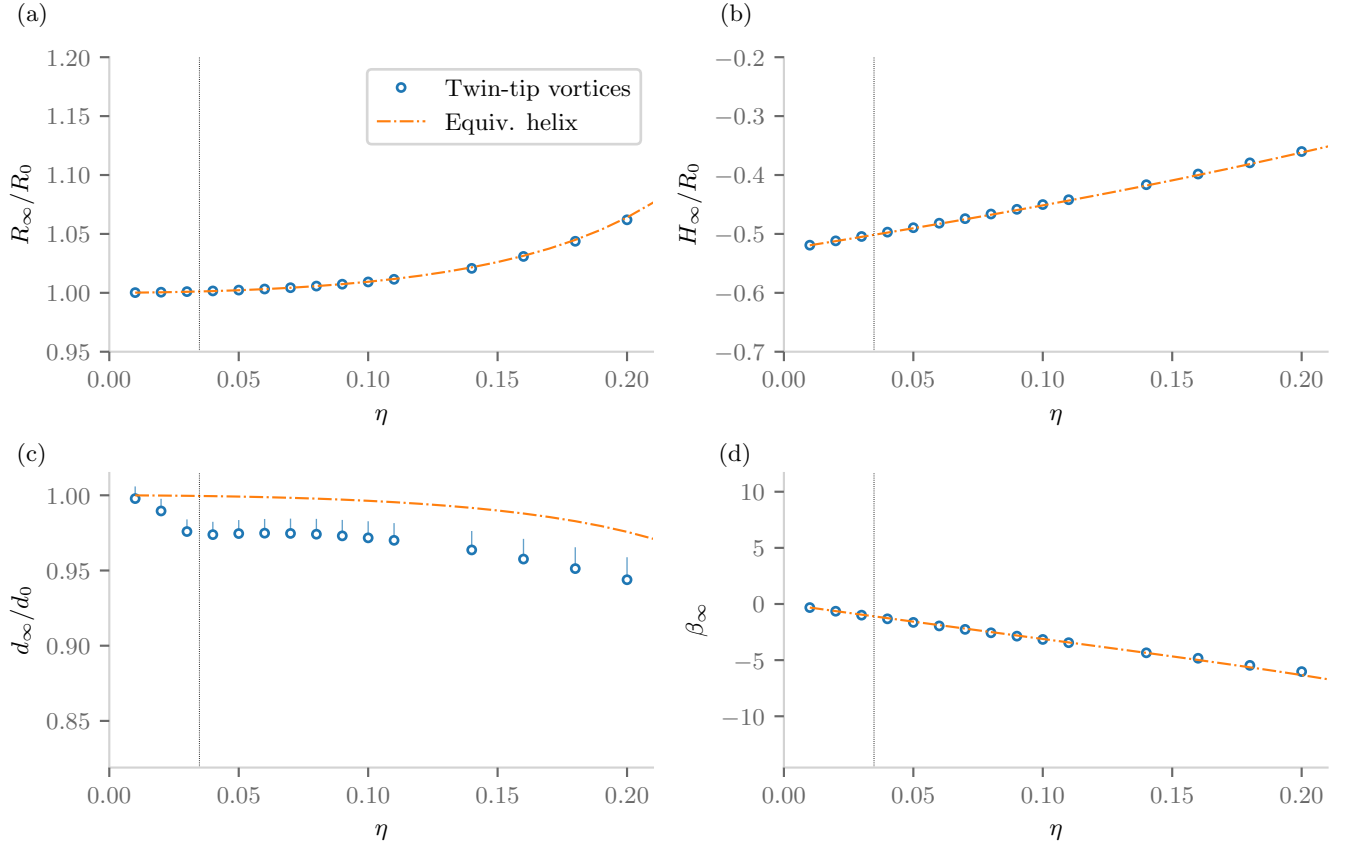


FIG. 20. Evolution of the far-wake parameters as a function of η for $\lambda = 2$ (wind turbine regime), $R_0^* = 9.5$ and $\varepsilon_0^* = 0.2$. Dashed lines correspond to the equivalent vortex approximations in (a,b) and to equations (29) and (30) in (c,d). For reference, fig. (c) also displays the minimum and maximum values of $d(\zeta)/d_0$ for $\zeta \rightarrow \infty$ as a vertical bar. The vertical dotted line in (c) indicates the value $\eta = \pi/(R_0^*)^2$ where $\beta_\infty \approx 1$.

solutions and their dependence with respect to the main parameters.

Because our solutions are based on a filament description, they do not provide information on the formation of the vortices in the neighborhood of the blade. We have assumed that well-defined and separated vortices are immediately formed behind the blade. Recent numerical simulations and experiments suggest the roll-up process to be significantly more complex for split-tip configurations [33, 34]. Our description does not account on the internal structure of the vortices either. Vortex cores are deformed by local effects, like curvature and torsion, and through the interaction with other vortices. These deformations are also the source of short-wavelength instabilities [35–37]. Taking into account these effects requires other numerical techniques [38] and different theoretical methods [39]. Helical solutions are known to be unstable with respect to a long-wavelength instability [40]. Similar instabilities are therefore expected here. In a follow-up paper [41], the linear stability of our solutions is analysed using the impulse response approach developed in [15]. Owing to the higher complexity of our solutions, we demonstrate that there exist different types of instability modes. As for the Widnall instability [42, 43], each instability mode is nevertheless shown to be associated with a specific pairing event.

ACKNOWLEDGMENT

This work received support from the French Agence Nationale de la Recherche under the ANR TWIN-HELIX project ANR-17-CE06-0018.

-
- [1] F. Gandhi and L. Tauszig, Influence of individual interactions on helicopter blade-vortex interaction noise, in *Proceedings of the 26th European Rotorcraft Forum* (2000).
 - [2] J. C. Hardin and S. L. Lamkin, Concepts for reduction of blade/vortex interaction noise, *J. Aircr.* **24**, 120 (1987).
 - [3] Y. H. Yu, Rotor blade-vortex interaction noise, *Prog. Aerosp. Sci.* **36**, 97 (2000).
 - [4] A. Brocklehurst and G. Barakos, A review of helicopter rotor blade tip shapes, *Prog. Aerosp. Sci.* **56**, 35 (2013).
 - [5] S. Ito, Aerodynamic influence of leading-edge serrations on an airfoil in a low Reynolds number, *J. Biomech. Sci. Eng.* **4**, 117 (2009).
 - [6] E. Pang, A. Cambray, D. Rezgui, M. Azarpeyvand, and S. A. Showkat Ali, Investigation towards a better understanding of noise generation from UAV propellers, in *2018 AIAA/CEAS Aeroacoustics Conference* (2018) p. 3450.
 - [7] J.-J. Chattot, Effects of blade tip modifications on wind turbine performance using vortex model, *Comput Fluids* **38**, 1405 (2009).
 - [8] A. Ebrahimi and R. Mardani, Tip-vortex noise reduction of a wind turbine using a winglet, *J. Energy Eng.* **144**, 04017076 (2018).
 - [9] A. Brocklehurst and A. Pike, Reduction of BVI noise using a vane tip, in *AHS Aeromechanics Specialists Conference* (American Helicopter Society, 1994).
 - [10] C. Copland, F. Coton, and R. M. Galbraith, An experimental study of the idealised vortex system of a novel rotor blade tip, *Aeronaut. J* **102**, 385 (1998).
 - [11] F. N. Coton, R. B. Green, and R. M. Galbraith, Analysis of model rotor blade pressures during parallel interaction with twin vortices, *J. Aircr.* **42**, 1552 (2005).
 - [12] C.-H. Cho, D.-J. Lee, C. Hwang, and Kari, Numerical investigations of parallel BVI noise with split tip vortices, in *AHS Internaitonal 62nd Annual Forum*, Vol. I (American Helicopter Society, 2006) pp. 13 – 19.
 - [13] J. Jung, W. Y. Choi, and S. Lee, Effect of the blade inner-tip position on the generation of twin vortices, *J. Aircr.* **45**, 728 (2008).
 - [14] J. N. Sørensen, Aerodynamic aspects of wind energy conversion, *Annu. Rev. Fluid Mech.* **43**, 427 (2011).
 - [15] E. Durán Venegas, P. Rieu, and S. Le Dizès, Structure and stability of Joukowski’s rotor wake model, *J. Fluid Mech.*, In press. (2021).
 - [16] S. W. Thomson, Xxiv. vibrations of a columnar vortex, *The London, Edinburgh, and Dublin Philosophical Magazine and Journal of Science* **10**, 155 (1880).
 - [17] L. S. Da Rios, Vortici ad elica, *Il Nuovo Cimento* (1911-1923) **11**, 419 (1916).
 - [18] M. Melander, N. Zabusky, and J. McWilliams, Symmetric vortex merger in two dimensions: causes and conditions, *J. Fluid Mech.* **195**, 303 (1988).
 - [19] P. Meunier, U. Ehrenstein, T. Leweke, and M. Rossi, A merging criterion for two-dimensional co-rotating vortices, *Phys. Fluids* **14**, 2757 (2002).
 - [20] C. Cerretelli and C. Williamson, The physical mechanism for vortex merging, *J. Fluid Mech.* **475**, 41 (2003).
 - [21] C. Josserand and M. Rossi, The merging of two co-rotating vortices: a numerical study, *Eur. J. Mech. B Fluids* **26**, 779 (2007).
 - [22] T. Leweke, S. Le Dizes, and C. H. Williamson, Dynamics and instabilities of vortex pairs, *Annu. Rev. Fluid Mech.* **48**, 507 (2016).
 - [23] F. Laporte and T. Leweke, Elliptic instability of counter-rotating vortices: experiment and direct numerical simulation, *AIAA Journal* **40**, 2483 (2002).
 - [24] P. Meunier, S. Le Dizès, and T. Leweke, Physics of vortex merging, *C R Phys* **6**, 431 (2005).
 - [25] P. Meunier and T. Leweke, Elliptic instability of a co-rotating vortex pair, *J. Fluid Mech.* **533**, 125 (2005).
 - [26] C. Roy, N. Schaeffer, S. Le Dizès, and M. Thompson, Stability of a pair of co-rotating vortices with axial flow, *Phys. Fluids* **20**, 094101 (2008).
 - [27] E. Durán Venegas and S. Le Dizès, Generalized helical vortex pairs, *J. Fluid Mech.* **865**, 523 (2019).
 - [28] P. G. Saffman, *Vortex dynamics* (Cambridge university press, 1992).
 - [29] J. Leishman, *Principles of Helicopter Aerodynamics*, Cambridge Aerospace Series (Cambridge University Press, 2016).
 - [30] H. Lamb, *Hydrodynamics*, Dover Books on Physics (Dover publications, 1945).
 - [31] N. E. Zhukovskii and V. P. Vetchinkin, *Théorie tourbillonnaire de l’hélice propulsive* (Gauthier-Villars, 1929).
 - [32] J. C. Hardin, The velocity field induced by a helical vortex filament, *Phys. Fluids* **25**, 1949 (1982).
 - [33] G. Narayan and B. John, Effect of winglets induced tip vortex structure on the performance of subsonic wings, *Aerospace Science and Technology* **58**, 328 (2016).
 - [34] D. Schröder, T. Leweke, R. Hörschemeyer, and E. Stumpf, Experiments on helical vortex pairs in the wake of a rotor, in *Proceedings of the AIAA Scitech 2021 Forum* (2021).
 - [35] R. R. Kerswell, Elliptical instability, *Annu. Rev. Fluid Mech.* **34**, 83 (2002).

- [36] F. J. Blanco-Rodríguez and S. Le Dizès, Elliptic instability of a curved Batchelor vortex, *J. Fluid Mech.* **804**, 224 (2016).
- [37] F. J. Blanco-Rodríguez and S. Le Dizès, Curvature instability of a curved Batchelor vortex, *J. Fluid Mech.* **814**, 397 (2017).
- [38] M. Brynjell-Rahkola and D. S. Henningson, Numerical realization of helical vortices: application to vortex instability, *Theor. Comp. Fluid Dyn* **34**, 1 (2020).
- [39] F. J. Blanco-Rodríguez, S. Le Dizès, C. Selçuk, I. Delbende, and M. Rossi, Internal structure of vortex rings and helical vortices, *J. Fluid Mech.* **785**, 219 (2015).
- [40] S. E. Widnall, The stability of a helical vortex filament, *J. Fluid Mech.* **54**, 641 (1972).
- [41] A. Castillo-Castellanos, E. Durán Venegas, and S. Le Dizès, Closely spaced co-rotating helical vortices: Long-wave instability, Manuscript submitted for publication (2021).
- [42] H. U. Quaranta, H. Bolnot, and T. Leweke, Long-wave instability of a helical vortex, *J. Fluid Mech.* **780**, 687 (2015).
- [43] H. U. Quaranta, M. Brynjell-Rahkola, T. Leweke, and D. S. Henningson, Local and global pairing instabilities of two interlaced helical vortices, *J. Fluid Mech.* **863**, 927 (2019).